


Magnetic antiskyrmions in two-dimensional van der Waals magnets engineered by layer stacking

Kai Huang,¹ Edward Schwartz,¹ Ding-Fu Shao,² Alexey A. Kovalev^{1,*} and Evgeny Y. Tsymbal^{1,†}

¹*Department of Physics and Astronomy & Nebraska Center for Materials and Nanoscience, University of Nebraska, Lincoln, Nebraska 68588-0299, USA*

²*Key Laboratory of Materials Physics, Institute of Solid-State Physics, HFIPS, Chinese Academy of Sciences, Hefei 230031, China*

 (Received 24 August 2023; revised 5 December 2023; accepted 2 January 2024; published 19 January 2024)

Magnetic skyrmions and antiskyrmions are topologically protected quasiparticles exhibiting a whirling spin texture in real space. Antiskyrmions offer some advantages over skyrmions as they are expected to have higher stability and can be electrically driven with no transverse motion. However, unlike the widely investigated skyrmions, antiskyrmions are rarely observed due to the required anisotropic Dzyaloshinskii-Moriya interaction (DMI). Here, we propose to exploit the recently demonstrated van der Waals (vdW) assembly of two-dimensional (2D) materials that breaks inversion symmetry and creates conditions for anisotropic DMI. Using a 2D vdW magnet CrI₃ as an example, we demonstrate, based on density-functional theory (DFT) calculations, that this strategy is a promising platform to realize antiskyrmions. Polar layer stacking of two centrosymmetric magnetic monolayers of CrI₃ efficiently lowers the symmetry, resulting in anisotropic DMI that supports antiskyrmions. The DMI is reversible by switching the ferroelectric polarization inherited from the polar layer stacking, offering the control of antiskyrmions by an electric field. Furthermore, we find that the magnetocrystalline anisotropy and DMI of CrI₃ can be efficiently modulated by Mn doping, creating a possibility to control the size of antiskyrmions. Using atomistic spin dynamics simulations with the parameters obtained from our DFT calculations, we predict the formation of antiskyrmions in a Cr_{0.88}Mn_{0.12}I₃ bilayer and switching their spin texture with polarization reversal. Our results open a direction to generate and control magnetic antiskyrmions in 2D vdW magnetic systems.

DOI: [10.1103/PhysRevB.109.024426](https://doi.org/10.1103/PhysRevB.109.024426)

I. INTRODUCTION

The discovery of magnetic skyrmions [1–6] has led to an increasing interest in magnetic quasiparticles exhibiting a whirling spin texture and nontrivial real-space topology [7–9]. The topological protection of these quasiparticles ensures their shape stability and makes them promising as potential information carriers in spintronic devices [10–12]. The topology of the magnetic quasiparticles is characterized by a topological charge [13], a nonvanishing integer describing the winding number of the classical spin when mapped on a unit sphere. The topological charge is associated with interesting physical phenomena, such as the topological Hall effect [14,15] and the skyrmion Hall effect [16–18] that can be used to detect the quasiparticles.

Among the topological quasiparticles are magnetic antiskyrmions. Antiskyrmions are analogs of skyrmions but have an opposite topological charge compared to a skyrmion with the same polarity [19]. The morphological difference between skyrmions and antiskyrmions comes from their symmetries. It is known that depending on the crystal symmetry, two distinct types of skyrmions can be observed, Bloch [2,3] and

Néel skyrmions [20]. Skyrmions, no matter Bloch type or Néel type, are always isotropic. As shown in Figs. 1(a) and 1(c), the spin spiral structure along x and y directions of a Néel-type skyrmion is the same. However, in antiskyrmions, the in-plane rotational symmetry is broken and the spin structures along the x and y directions have opposite chiralities and contain alternating Bloch- and Néel-type spin twists [19,21] [Figs. 1(b) and 1(d)].

Skyrmions and antiskyrmions are typically stabilized by Dzyaloshinskii-Moriya interaction (DMI)—an antisymmetric exchange interaction between adjacent magnetic moments that favors their perpendicular alignment [22,23]. The DMI between spins \vec{S}_α and \vec{S}_β takes the form

$$E_{\text{DMI}} = \vec{d}_{\alpha\beta} \cdot (\vec{S}_\alpha \times \vec{S}_\beta), \quad (1)$$

where $\vec{d}_{\alpha\beta}$ is the DMI vector. The DMI energy is controlled by symmetry of the system and spin-orbit coupling. It requires broken-inversion symmetry (which is a necessary but not sufficient condition) and can be isotropic or anisotropic. In thin-film structures the isotropic DMI leads to skyrmions [Figs. 1(a) and 1(c)], while the anisotropic DMI with opposite signs along perpendicular x and y directions can stabilize antiskyrmions [Figs. 1(b) and 1(d)].

The requirement of the anisotropic DMI makes observing magnetic antiskyrmions more difficult. Nevertheless, recently

*alexey.kovalev@unl.edu

†tsymbal@unl.edu

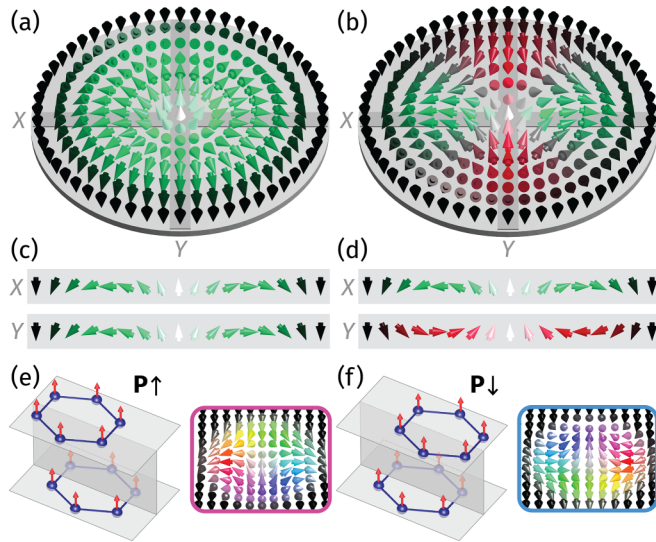


FIG. 1. (a), (b) Schematic of a Néel-type skyrmion (a) and antiskyrmion (b). Brightness of each arrow represents an out-of-plane spin component with a bright (dark) contrast indicating spin pointing up (down). Color represents the chirality of spin rotation along the diameter in the specific direction, where green (red) color indicates clockwise (counterclockwise) rotation. (c), (d) Spin rotation of the skyrmion (c) and antiskyrmion (d) along the diameter in x and y directions. (e), (f) Schematic of 2D ferromagnetic bilayers engineered to have polar stackings with ferroelectric polarization pointing up $P \uparrow$ (e) or down $P \downarrow$ (f). Red arrows indicate magnetic moments. Polarization switching changes the spin texture of magnetic antiskyrmions.

there have been a few experimental demonstrations of antiskyrmions in noncentrosymmetric magnets of D_{2d} [24–26] and S_4 [27] point-group symmetries. Theoretical analyses indicate that antiskyrmions may have some advantages over their isotropic counterparts. In particular, antiskyrmions are expected to have stronger stability due to the reduced magnetostatic energy [28]. In addition, antiskyrmions can be driven by charge currents without a transverse motion due to the skyrmion Hall effect, which may be beneficial from the point of view of applications in racetrack memories [19,29].

Two-dimensional (2D) van der Waals (vdW) ferromagnets [30–33] have recently emerged as novel skyrmionic hosts. In these materials, which are all centrosymmetric, space-inversion symmetry breaking required for DMI can be realized by the interface proximity effect in a vdW heterostructure [34,35]. This allows the stabilization of magnetic skyrmions in a system with minimum thickness and even in the absence of the external magnetic field, as has been demonstrated in the recent experiments [36–40].

Besides the interface proximity effect, recent advances in vdW assembly techniques showed that interlayer stacking can be used to control properties of vdW materials. It has been demonstrated that minor interlayer sliding [41,42] or small-angle interlayer twisting [43–45] can generate electronic and transport responses of 2D materials which do not exist in the bulklike phase. Specifically, a combination of 180° rotation of the top monolayer followed by interlayer sliding results in a noncentrosymmetric stacking pattern [Figs. 1(e) and 1(f)].

This is accompanied by the emergence of an out-of-plane electric polarization reversible by an external electric field through interlayer sliding [46–48]. This approach allows the design of synthetic 2D ferroelectrics (and multiferroics) out of parent nonpolar compounds and to uncover functionalities not existent in the bulk phase (e.g., Ref. [49]).

Applying this approach to 2D vdW ferromagnets allows breaking inversion symmetry and thus providing the prerequisite for DMI. In addition, sliding away from the mirror-symmetric stacking to a more energetically favorable stacking breaks the in-plane rotational symmetry of the 2D crystal, producing anisotropy of the DMI that is required for antiskyrmions. The switching of ferroelectric polarization by an applied electric field through interlayer sliding is expected to reverse the DMI sign, providing a possibility of a non-volatile electric-field control of antiskyrmions.

Among 2D vdW magnets, CrI_3 appears to be a viable material to exhibit antiskyrmions when it is engineered to be polar. CrI_3 was one of the first vdW magnets exfoliated down to a monolayer [31] and extensively studied afterwards [50–52]. It has out-of-plane magnetic anisotropy required for magnetic (anti)skyrmions. The heavy I atoms are expected to provide a large DMI when symmetry allows. In fact, theoretical calculations have predicted the formation of magnetic skyrmions in a CrI_3 monolayer in the presence of a strong external electric field [53] or defects [54]. Last, CrI_3 is an insulator, which allows applying a sufficiently large electric field across a polar CrI_3 bilayer to switch its ferroelectric polarization.

In this work, using first-principles density-functional theory (DFT) calculations, we explore the possibility to realize magnetic antiskyrmions in a ferroelectric CrI_3 bilayer engineered by layer stacking. We demonstrate that the polar layer stacking leads to anisotropic DMI, which can be switched by reversal of ferroelectric polarization. Further, we show that Mn doping of CrI_3 is favorable for magnetic antiskyrmions to occur in a polar $\text{Cr}_{1-x}\text{Mn}_x\text{I}_3$ bilayer due to the reduced magnetic anisotropy and enhanced DMI. Our atomistic spin dynamics simulations with the parameters obtained from the DFT calculations predict the formation of antiskyrmions in a $\text{Cr}_{0.88}\text{Mn}_{0.12}\text{I}_3$ bilayer and switching their spin texture with polarization reversal. These results demonstrate an approach to generate magnetic quasiparticles in 2D vdW magnets and control their spin texture by electric fields.

II. SYMMETRY ANALYSIS

CrI_3 is a 2D vdW ferromagnetic insulator with an easy axis along the [001] direction (z axis). At low temperature, bulk CrI_3 is stabilized in a rhombohedral structure of space group $R\bar{3}$ [55]. The bulk unit cell contains three CrI_3 monolayers stacked in the [001] direction with Cr atoms surrounded by a distorted edge-sharing octahedron of six I atoms [Fig. 2(a)]. The Cr–I–Cr bond angle between the CrI_6 octahedra is nearly 90° , leading to the superexchange interaction that favors a ferromagnetic intralayer coupling [56,57]. The presence of inversion symmetry in bulk CrI_3 prohibits a finite DMI, and hence magnetic quasiparticles are not expected to emerge in bulk CrI_3 . The same conclusion is valid for monolayer CrI_3 , whose structure belongs to centrosymmetric magnetic space group $P\bar{3}1m'$, and thus prohibits DMI. There-

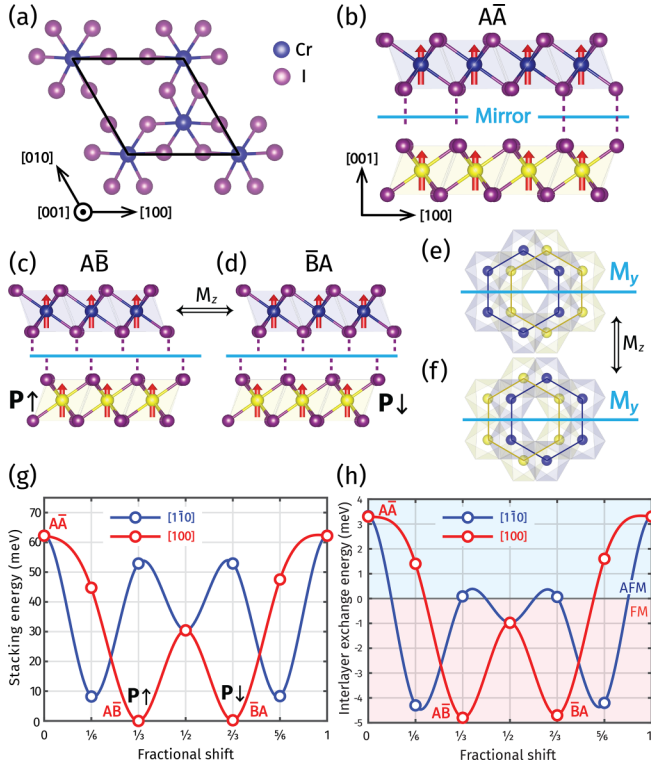


FIG. 2. (a) Top view of monolayer CrI_3 . (b) Side view of AA stacking configuration of bilayer CrI_3 constructed by mirroring (M_z) of the bottom monolayer (yellow) to top (blue). (c), (d) AB (c) and BA (d) stacking configurations of bilayer CrI_3 obtained from AA by $\mp a/3$ translation of the top monolayer. They correspond to opposite ferroelectric polarizations ($P\uparrow$ and $P\downarrow$) and can be swapped by M_z symmetry transformation. (e), (f) Top views of (c), (d), respectively. Only the Cr honeycomb lattice is shown. (g), (h) Stacking energy (g) and interlayer exchange energy (h) as functions of lateral translation along $[100]$ (blue) and $[1\bar{1}0]$ (red) directions with respect to the AA stacking.

fore, an interface proximity effect or an external electric field [53] are typically considered as means to break inversion symmetry and create conditions for the appearance of topological magnetic quasiparticles.

Here, we explore a different approach where the polar stacking technique is used to break inversion symmetry. First, a CrI_3 bilayer is formed in such a way that the top monolayer \bar{A} is assembled as a mirror reflection M_z of the bottom monolayer A with respect to the (001) plane [Fig. 2(b)]. This stacking, denoted by AA , is related to the bulklike stacking of a CrI_3 bilayer by 180° rotation of the top monolayer about the z axis. While this stacking breaks the inversion symmetry, it does not produce DMI in the 2D system due to M_z symmetry. The AA structure is, however, usually energetically unfavorable. It spontaneously relaxes to a more favorable AB (or BA) stacking through translation of the top monolayer layer along the $[100]$ direction (x axis) by $\pm a/3$, where a is a lattice constant [Figs. 2(c) and 2(d)]. Under this translation, the magnetic space group of the bilayer is lowered from $P\bar{3}1m'$, to Cm' . The translation along the x axis not only breaks mirror symmetry M_z , but also breaks in-plane rotational C_3 symmetry, leading to anisotropic DMI.

To analyze the layer stacking effect on DMI and the spin texture, it is convenient to express the DMI energy in the form of a continuous model [58,59]:

$$E_{\text{DMI}} = \sum_{ij} D_{ij} \hat{e}_i \cdot (\vec{m} \times \nabla_j \vec{m}), \quad (2)$$

where D_{ij} is the DMI tensor with indexes $i, j \in x, y, z$; \hat{e}_i is a unit vector; and \vec{m} is the unit vector along the magnetization direction. The form of the DMI tensor D_{ij} is determined by the crystallographic symmetry of the system. The CrI_3 monolayer structure belongs to point group D_{3d} , where all D_{ij} components must be zero due to space-inversion symmetry, resulting in a trivial spin texture. The same is true for the AA stacked bilayer due to M_z symmetry. In the presence of an external electric field applied in the z direction, the D_{3d} symmetry of a CrI_3 monolayer is reduced to C_{3v} , which allows for two nonzero tensor components related by $D_{xy} = -D_{yx}$. Such DMI can stabilize Néel-type skyrmions [53]. The symmetry is further reduced for the polar AB (BA) stacking, where the only remaining symmetry operation is mirror reflection M_y [Figs. 2(e) and 2(f)]. This symmetry permits the nondiagonal D_{ij} components D_{xy} , D_{yx} , D_{yz} , and D_{zy} to be nonzero and mutually independent (see Supplemental Material [60] for details and Ref. [61] for a more general discussion). For a 2D system, however, we can assume that there is no magnetic moment variation along the z direction resulting in $D_{yz} = 0$. Also, our calculations predict that D_{zy} is small compared to D_{xy} and D_{yx} and therefore we ignore its contribution for our further analysis. These assumptions restrict the summation in Eq. (2) to $i, j \in x, y$.

According to Eq. (2), each D_{ij} component corresponds to a spin spiral state along j direction in the 2D system and the chirality of the spiral is defined by the sign of D_{ij} . Opposite sign of D_{xy} and D_{yx} favors the same spin spiral chirality along the x and y directions resulting in a skyrmion [Figs. 1(a) and 1(c)], while the same sign of D_{xy} and D_{yx} favors opposite spin spiral chirality along the x and y directions resulting in an antiskyrmion [Figs. 1(b) and 1(d)]. If $|D_{xy}| = |D_{yx}|$, both skyrmions and antiskyrmions are expected to be circular, while if $|D_{xy}| \neq |D_{yx}|$, they can become elliptical. Elliptical skyrmions have been experimentally observed in systems with anisotropic DMI (e.g., Ref. [62]).

III. COMPUTATIONAL METHODS

Our calculations are based on DFT and employ the Vienna *ab initio* Simulation Package (VASP) [63], utilizing the projector augmented-wave method [64] and generalized gradient approximation with the PBEsol exchange-correlation functional [65]. A plane-wave cutoff energy of 500 eV is used in the calculations. All the atomic coordinates are relaxed until the force on each atom is less than $0.001 \text{ eV}/\text{\AA}$. To account for strong electronic correlations, a Hubbard onsite Coulomb parameter $U = 3 \text{ eV}$ is applied for the Cr atoms within a rotationally invariant DFT+ U approach [66]. The validity of the calculation method is checked by the lattice constant of the bulk CrI_3 . The calculated lattice constants for the low-temperature rhombohedral state and high-temperature monoclinic state of bulk CrI_3 are determined to be 6.894 and 6.813 \AA , respectively. These values are close to the experi-

ment values 6.867 and 6.866 Å [55]. We then construct an AB-stacked CrI₃ bilayer by extracting two monolayers from the low-temperature bulk phase and adding a vacuum layer of 30 Å in the out-of-plane direction. The bilayer structure is fully relaxed with an $8 \times 8 \times 1$ k -point mesh in the irreducible Brillouin zone. The resulting lattice constant is found to be 6.892 Å.

In the investigation of the stacking order of dipole bilayer CrI₃, the in-plane lattice constant of the cell is fixed to 6.892 Å, which corresponds to the lattice constant of AB-stacking CrI₃ bilayer. The atomic positions within the cell are then relaxed. The dipole correction is included in calculations to eliminate the spurious electric field in the vacuum layer. In the calculation of magnetic anisotropy and DMI, spin-orbit coupling is applied. In the calculations involving Cr_{1-x}Mn_xI₃ within virtual crystal approximation (VCA) the dipole correction is disabled to facilitate convergence. This choice does not significantly impact the results, as the dipole moment per unit area of 0.176 pC/m is considered to be small.

The atomistic spin dynamics modeling is performed using the VAMPIRE code [67]. To conduct simulations, a supercell of polar bilayer CrI₃ (Cr_{1-x}Mn_xI₃) with dimensions of 70 nm × 70 nm is generated. Nonmagnetic I atoms are ignored, and only a magnetic atom honeycomb lattice is considered. The periodic boundary conditions are applied. The simulation starts with the setup of a circular ferromagnetic domain located at the center of the supercell, where the magnetic moments are initially oriented along the + z (- z) directions inside (outside) the domain wall. Then, the Landau-Lifshitz-Gilbert (LLG) equation is solved iteratively over time steps. Time interval for each step is chosen to be 10^{-15} s and totally about 5×10^6 steps are used to reach the quasiparticle state equilibrium. During the simulation, the round domain can gradually relax, transforming into a stable magnetic quasiparticle, or it may shrink and eventually disappear, assimilating into the background. In the calculations, for faster convergence of the spin structure to the equilibrium, the Gilbert damping constant is chosen to be $\alpha_G = 2$.

IV. PRISTINE CrI₃ BILAYER

First, we ascertain that the ground state of bulk CrI₃ is predicted correctly. We find the magnetic moment of Cr atoms in the rhombohedral low-temperature bulk state is $m(\text{Cr}) = 3.32 \mu_B$. Using the standard four-state methodology (e.g., Ref. [68]), we calculate the intralayer Heisenberg exchange interaction between Cr atoms and obtain $J_{\text{intra}}^{\text{NN}} = 1.81$ meV for nearest neighbors and $J_{\text{intra}}^{\text{NNN}} = 0.23$ meV for next-nearest neighbors, supporting in-plane ferromagnetic ordering of CrI₃. (Note that we define the exchange energy between two moments \vec{s}_1 and \vec{s}_2 by $E_{\text{ex}} = -2J\vec{s}_1 \cdot \vec{s}_2$.) The magnetic anisotropy energy (MAE) per Cr atom is found to be 0.72 meV. All these results are consistent with the previous calculations [69–74].

A polar bilayer is constructed by mirroring the bottom monolayer CrI₃ to the top. To find the ground state of the bilayer, we calculate the total energy as a function of the lateral alignment of the two monolayers. For each stacking configuration, the atomic structure of the bilayer is relaxed. As shown in Fig. 2(g), two energy minima appear when the top mono-

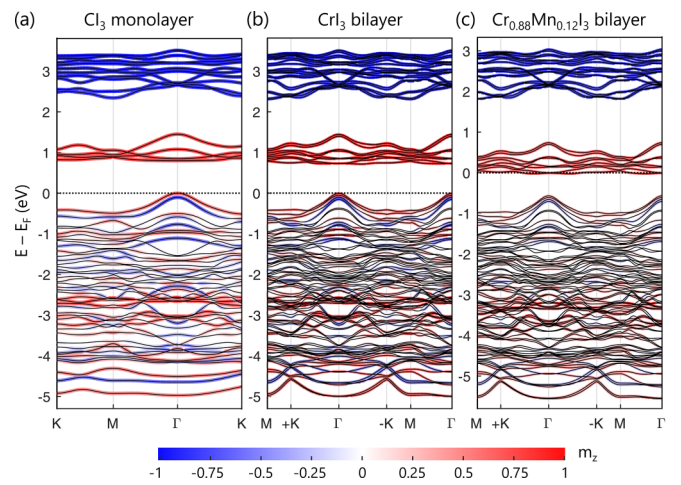


FIG. 3. (a), (b), (c) Band structure of a CrI₃ monolayer (a), a CrI₃ polar bilayer (b) and a Cr_{0.88}Mn_{0.12}I₃ polar bilayer (c) calculated in the presence of spin-orbit coupling. Spin projection to the direction of magnetization m_z is shown in color. The horizontal dashed line indicates the Fermi energy (E_F).

layer is translated along the [100] direction with respect to the bottom monolayer, and three—when it is translated along the $[1\bar{1}0]$ direction. As is evident from this plot, the M_z -symmetric A \bar{A} stacking is unstable with respect to the lateral displacements. Two global energy minima appear at the $a/3$ and $2a/3$ translations along the [100] direction ($\pm a/3$, when periodic boundary conditions are applied), corresponding to the A \bar{B} and $\bar{B}A$ stacking configurations. M_z symmetry is broken for these structures which makes them polar with the A \bar{B} stacking having polarization up ($P \uparrow$, i.e., along the + z direction) and the $\bar{B}A$ stacking having polarization down ($P \downarrow$, i.e., along the - z direction). The two polar ground-state structures, A \bar{B} and $\bar{B}A$, are related by M_z -symmetry transformation. Therefore, polarization switching of the bilayer is equivalent to the $\pm a/3$ lateral translation of one monolayer with respect to the other along the [100] direction (or equivalently along the [010] direction). The corresponding dipole moment per area for the polar structures is estimated to be 0.176 pC/m.

We find that the intralayer exchange coupling in a CrI₃ bilayer is nearly insensitive to the lateral alignment of the two monolayers favoring a ferromagnetic order. This is however not the case for the interlayer coupling which, due to its small magnitude, strongly depends on the layer stacking. Figure 2(h) shows the results of our computations. It is seen that while the A \bar{A} stacking favors antiferromagnetic coupling with the Heisenberg exchange energy of about 3 meV per Cr atom, the polar A \bar{B} and $\bar{B}A$ ground-state stacking exhibits ferromagnetic coupling of about 5 meV per Cr atom. These results are reminiscent of those found previously for a centrosymmetric CrI₃ bilayer [75] where the stacking-dependent magnetism was explained by a competition of the different interlayer orbital hybridizations. This fact indicates that while the polar stacking is essential for the appearance of nonvanishing DMI, it does not affect much the intralayer exchange coupling. Based on these results, in the following discussion, we assume that a polar A \bar{B} ($\bar{B}A$)-stacked CrI₃ bilayer has all ferromagnetic order.

TABLE I. Magnetic parameters for bulk CrI₃, polar bilayer CrI₃ ($P \uparrow$) and 12% Mn-doped CrI₃ ($P \uparrow$): magnetic moment (m), intralayer exchange coupling ($J_{\text{intra}}^{\text{NN}}$ and $J_{\text{intra}}^{\text{NNN}}$), magnetic stiffness (A), magnetocrystalline anisotropy (K), DMI vectors ($|\vec{d}_1|$ and $|\vec{d}_2|$), and D_{xy} and D_{yx} components of the DMI tensor. The exchange interaction energy is defined by $E_{\text{ex}} = -2J\vec{s}_1 \cdot \vec{s}_2$.

Parameter	CrI ₃ (bulk)	CrI ₃ (polar bilayer)	Cr _{0.88} Mn _{0.12} I ₃ (polar bilayer)
m (μ_B)	3.32	3.31	3.43 (Cr) 3.66 (Mn)
$J_{\text{intra}}^{\text{NN}}$ (meV)	1.81	1.70	2.05
$J_{\text{intra}}^{\text{NNN}}$ (meV)	0.23	0.29	0.27
A (pJ/m)	1.21	1.28	1.50
K (meV)	0.72	0.67	0.03
K (MJ/m ³)	0.84	0.77	0.04
$ \vec{d}_1 $ (meV)	0	0.04	0.08
$ \vec{d}_2 $ (meV)	0	0.05	0.13
D_{xy} (mJ/m ²)	0	-0.003	-0.067
D_{yx} (mJ/m ²)	0	-0.009	-0.087

Figure 3(b) shows the calculated band structure of a polar bilayer CrI₃. Due to a relatively weak orbital hybridization across the interface, the electronic bands of the bilayer are similar to those of a monolayer [Fig. 1(a)]. There are, however, visible differences between the bands around the $+K$ and $-K$ points for the bilayer but not for the monolayer. This is due to the broken space-inversion symmetry of the bilayer that lifts band degeneracy for positive and negative wave vectors. Overall, the band structure of the bilayer is largely determined by the crystal-field splitting of the $3d$ orbitals of the Cr³⁺ ion into the triply degenerate t_{2g} states that lie at a lower energy and the doubly degenerate e_g states that lie at a higher energy [bands around 1 eV in Figs. 3(a) and 3(b)]. According to Hund's rule, the majority-spin t_{2g} states are fully occupied by the three available Cr³⁺ electrons and form the valence band, while the majority-spin e_g states form the low-energy conduction band. This picture is somewhat altered by the hybridization between the majority- and minority-spin bands driven by spin-orbit interaction, as well as by the Cr-I bonding that is seen from the orbital-resolved density of states in Fig. S1. Due to a large exchange splitting of the Cr spin bands, the minority-spin t_{2g} and e_g states are empty and lie at a higher energy [bands around 3 eV in Figs. 3(a) and 3(b)].

Table I displays the calculated magnetic parameters for the polar CrI₃ bilayer in comparison to those obtained for bulk CrI₃. We find that the magnetic moment of a Cr atom, the intralayer exchange coupling, and magnetocrystalline anisotropy do not change much by polar stacking. This is due to a weak interaction between CrI₃ monolayers so that stacking order does not influence the magnetic properties much. The critical difference occurs, however, in the DMI, which changes from a zero value in bulk CrI₃ to nonzero in a polar bilayer.

Here, the calculation of DMI has been performed based on the following arguments. Microscopically, DMI arises from the interaction of two magnetic atoms mediated by a nonmagnetic atom. As a result, the DMI vector in Eq. (1), is given by $\vec{d}_{\alpha\beta} = d_{\alpha\beta}(\hat{r}_\alpha \times \hat{r}_\beta)$, where \hat{r}_α and \hat{r}_β are the unit bond vectors between a nonmagnetic atom and magnetic atoms α and β , respectively. In our case, two magnetic Cr atoms are coupled through a nonmagnetic I atom via superexchange

interaction. Based on the Cm' symmetry of the system, we find two independent DMI vectors, \vec{d}_1 and \vec{d}_2 , that control the DMI between adjacent Cr atoms [75,76]. For a CrI₃ monolayer, each of these DMI vectors can be viewed as the sum of two contributions arising from a superexchange interaction between two Cr atoms and top and bottom I atoms. For example, in Fig. 4(a), the vector \vec{d}_1 characterizing DMI between Cr₀ and Cr₁ magnetic moments is given by the sum of vectors \vec{d}_{1a} and \vec{d}_{1b} associated with the superexchange interaction of the Cr atoms via top atom I_a and bottom atom I_b, respectively. Similarly, the DMI vector \vec{d}_2 that couples Cr₀ and Cr₂ moments is given by $\vec{d}_2 = \vec{d}_{2a} + \vec{d}_{2b}$. In Fig. 4(b), we plot all \vec{d}_1 and \vec{d}_2 vectors associated with each pair of Cr atoms in a Cr hexagon according to symmetry. It is seen that the \vec{d}_1 vectors (shown in red) lie off the mirror plane M_y while the \vec{d}_2 vectors (shown in yellow) lie in that plane. More details of the DMI analysis can be found in Supplemental Material [60].

The DMI vectors are calculated using the spin spiral method, where each component of \vec{d}_1 and \vec{d}_2 is obtained from the energy difference between specific spin configurations with a clockwise (CW) and counterclockwise (CCW) spiral.

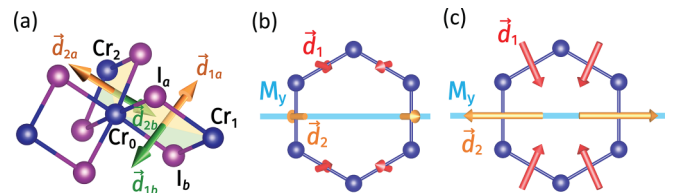


FIG. 4. (a) Construction of DMI vectors. DMI between Cr₀ and Cr₁ magnetic moments is determined by vector \vec{d}_1 given by the sum of vectors \vec{d}_{1a} and \vec{d}_{1b} resulting from the superexchange interaction of the Cr atoms with top atom I_a and bottom atom I_b. Similarly, the DMI vector \vec{d}_2 that couples Cr₀ and Cr₂ moments is given by $\vec{d}_2 = \vec{d}_{2a} + \vec{d}_{2b}$. (b), (c) DMI vectors \vec{d}_1 and \vec{d}_2 associated with pairs of Cr atoms connected by gray lines on a Cr honeycomb lattice for CrI₃ (a) and Cr_{0.88}Mn_{0.12}I₃ (b) polar bilayers. The DMI vectors in (b) and (c) are depicted in the same scale.

For example, as shown in Supplemental Material [60],

$$d_{1x} = \frac{E_{CCW} - E_{CW}}{32S^2}, \quad (3)$$

where S is the spin momentum. In the calculations, we construct the spin spirals assuming for simplicity that two monolayers of CrI_3 in a bilayer can be treated as one, which implies averaging of \vec{d}_1 and \vec{d}_2 over the two monolayers. The calculated DMI vectors \vec{d}_1 and \vec{d}_2 are depicted in Fig. 4(b) and their values are listed in Table I. The results show, as expected, that the in-plane rotational symmetry of the DMI in a bilayer is broken. As seen from Fig. 4(b), the four DMI vectors \vec{d}_1 at sides of the Cr atom hexagon are centripetal, while the two DMI vectors \vec{d}_2 are centrifugal.

The obtained DMI vectors are related to the anisotropic DMI tensor in Eq. (2) as follows:

$$D_{ij} = \frac{1}{V_{uc}} \sum_{\alpha, \beta} S^2 d_{\alpha\beta, i} r_{\alpha\beta, j}, \quad (4)$$

where α, β represents different atoms in the unit cell, V_{uc} is the volume of the unit cell, $d_{\alpha\beta, i}$ is the i component of the DMI vector between atom α and β , and $r_{\alpha\beta, j}$ is the j component of the displacement vector from atom α to β . Using Eq. (1), we obtain two nonvanishing components of the DMI tensor: $D_{xy} = -0.003 \text{ mJ/m}^2$ and $D_{yx} = -0.009 \text{ mJ/m}^2$. D_{xy} and D_{yx} have the same sign, indicating opposite spin spiral chiralities along the x and y directions, and, therefore, their combination is expected to be favorable for magnetic antiskyrmions.

We find, however, that the obtained parameters for the polar CrI_3 bilayer do not support any magnetic quasiparticles due to a relatively large MAE and a relatively small DMI. This can be seen from our theoretical analysis of the size and shape of skyrmions (antiskyrmions) given in Supplemental Material [60]. We find that an (anti)skyrmion has an elliptical shape with a radius that can be estimated as follows:

$$R = \pi D \sqrt{\frac{A'}{16A'K^2 - \pi^2 KD^2}}, \quad (5)$$

where $D = 1/2(\alpha|D_{xy}| + |D_{yx}|)$, $A' = 1/2(1 + \alpha^2)A$, and α is the ratio of the minor to major axes of the ellipse. For not too strong anisotropy of the DMI, the latter is given by $\alpha = \sqrt{1 + \epsilon^2}$, where

$$\epsilon^2 \approx \frac{\pi^2 |D_{xy}^2 - D_{yx}^2|}{64AK - 1/2\pi^2(|D_{xy}| + |D_{yx}|)^2}. \quad (6)$$

Equation (5) is valid when the (anti)skyrmion radius R is larger than the domain-wall width w , i.e., $R \gg w$, where $w = \frac{\pi D}{4K}$. In the limit of the isotropic DMI ($\alpha = 1$), Eq. (5) is reduced to the result obtained in Ref. [77]. Using Eq. (5), where for simplicity we assume $\alpha = 1$, we obtain the antiskyrmion size of 0.06 \AA , which is too small to exist. According to Eq. (5), to realize a sizable antiskyrmion, a weaker MAE and/or stronger DMI are necessary.

V. Mn-DOPED CrI_3 BILAYER

We propose to use substitutional doping of CrI_3 with Mn as a means to decrease MAE. MnI_3 is a vdW transition-metal

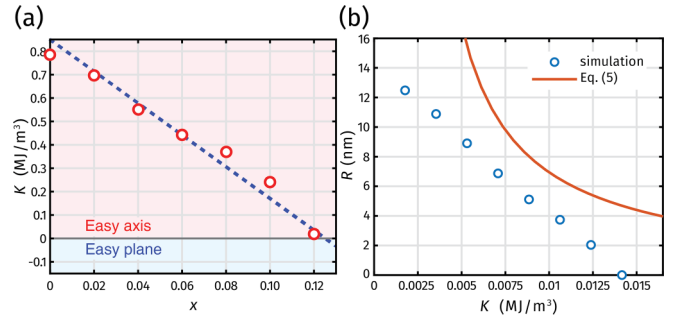


FIG. 5. (a) Calculated magnetic anisotropy K of a $\text{Cr}_{1-x}\text{Mn}_x\text{I}_3$ polar bilayer as a function of Mn doping x (red circles). The blue dashed line represents a linear interpolation of K between pure CrI_3 and MnI_3 . (b) Antiskyrmion radius R in a $\text{Cr}_{0.88}\text{Mn}_{0.12}\text{I}_3$ polar bilayer as a function of K obtained from spin dynamics simulations (blue dots) and estimated using Eq. (5) (orange curve).

trihalide with a structure similar to CrI_3 . It exhibits a strong magnetic anisotropy in the easy plane [78], which opposes the easy-axis anisotropy of CrI_3 . Our calculations predict that MAE of a MnI_3 bilayer in the AB stacking configuration is -5.9 meV per Mn atom, compared to 0.67 meV per Cr atom in a polar CrI_3 bilayer. Additionally, the lattice constant of MnI_3 , as determined in our calculations, is 6.73 \AA , which is close to the lattice constant of CrI_3 of 6.89 \AA . Therefore, substitutional Mn doping of CrI_3 is feasible experimentally and can be used to make the magnetic anisotropy sufficiently small at a specific mixing ratio.

To calculate the electronic structure and MAE of $\text{Cr}_{1-x}\text{Mn}_x\text{I}_3$ as a function of Mn doping concentration x , we use virtual crystal approximation. Within VCA, the $\text{Cr}_{1-x}\text{Mn}_x$ substitutional disorder is treated assuming that the Cr-site position in CrI_3 is occupied by a fictitious atom with atomic number $24(1-x) + 25x$, so that at $x = 1$, and the Mn-doped CrI_3 corresponds to pure MnI_3 . With increasing the Mn doping concentration x , the electronic structure of $\text{Cr}_{1-x}\text{Mn}_x\text{I}_3$ changes due to additional valence electrons that occupy the majority-spin e_g band. As a result, the Fermi energy (E_F) is pushed to the conduction band, and the band gap separating the e_g and t_{2g} states gets reduced [Fig. 3(c)] at a moderate x and disappears at $x = 1$ (Fig. S1 [60]).

As expected and evident from Fig. 5(a), an increase of the Mn doping concentration leads to a decrease of MAE per magnetic atom (K). At the doping range from $x = 0$ to $x = 0.12$, the anisotropy changes linearly with x , nearly reproducing the trend which is expected from the linear interpolation of $K(x)$ from $x = 0$ (CrI_3) to $x = 1$ (MnI_3) [the blue dashed line in Fig. 5(a)]. At $x = 0.12$, we obtain a sufficiently small $K = 0.03 \text{ meV}$. Therefore, we choose $\text{Cr}_{0.88}\text{Mn}_{0.12}\text{I}_3$ as a promising candidate to find antiskyrmions.

We note that the reduction of MAE with Mn doping can be explained in terms of the imbalance in the population of different p orbitals of the I atoms. It is known that nonmetallic I atoms control the MAE in CrI_3 due to the strong spin-orbit coupling associated with them. The sizable out-of-plane magnetic anisotropy of CrI_3 can be understood in terms of the second-order perturbation theory by the large contribution of the matrix elements of the orbital momentum between the un-

occupied p_x (p_y) and occupied p_y (p_x) states, while transitions to (from) the p_z states contribute to the in-plane anisotropy [79]. Due to the strong hybridization between the unoccupied transition-metal e_g states and I- p states, population of the former with Mn doping also leads to population of the latter. However, there is a disbalance in the population of the p_z and p_x (p_y) orbitals, due to the p_z states lying at a lower energy, as a result of their weaker bonding with the transition-metal e_g states (inset in Fig. S1 [60]). A larger population of the p_z states with doping leads to transitions between the occupied p_z states and unoccupied p_x (p_y) states, contributing to the in-plane anisotropy.

The calculated magnetic parameters are listed in Table I. We see that with Mn doping of $x = 0.12$, in addition to significant reduction of magnetic anisotropy, there is an enhancement of the Cr magnetic moment compared to the no-doping case. This is expected due to the additional majority-spin e_g electrons brought by Mn doping. In addition, we observe that the nearest-neighbor intralayer exchange coupling $J_{\text{intra}}^{\text{NN}}$ and the magnetic stiffness A supporting ferromagnetic ordering are increased with the doping. This is because the doped e_g electrons enhance the superexchange interaction [80]. This result is in agreement with the previous calculations suggesting the enhancement of the ferromagnetic exchange with electron doping of CrI_3 [81].

We find that the DMI in the $\text{Cr}_{0.88}\text{Mn}_{0.12}\text{I}_3$ polar bilayer is significantly enhanced compared to CrI_3 , as seen from the comparison of Figs. 4(c) and 4(b). As evident from Table I, in $\text{Cr}_{0.88}\text{Mn}_{0.12}\text{I}_3$, the absolute values of \vec{d}_1 and \vec{d}_2 are 0.08 and 0.13 meV, respectively. According to Eq. (3), the DMI tensor is represented by two nonvanishing components: $D_{xy} = -0.067$ meV and $D_{yx} = -0.087$ meV, which are an order of magnitude larger than the respective values for CrI_3 (Table I). Similar to the ferromagnetic superexchange interaction, this increase in DMI is driven by a stronger Cr-I bonding that is enhanced by the doped e_g electrons. Both components of the DMI are negative and thus are expected to support antiskyrmions.

VI. SPIN DYNAMICS SIMULATIONS

To explore the emergence of antiskyrmions in a polar $\text{Cr}_{1-x}\text{Mn}_x\text{I}_3$ bilayer, we perform atomistic spin dynamics simulations using the LLG equation:

$$\frac{\partial \vec{m}_i}{\partial t} = -\gamma (\vec{m}_i \times \vec{H}_i) + \alpha_G \left(\vec{m}_i \times \frac{\partial \vec{m}_i}{\partial t} \right). \quad (7)$$

Here, α_G is the Gilbert damping constant, γ is the gyromagnetic ratio, and $\vec{m}_i = \frac{\vec{M}_i}{|\vec{M}_i|}$ is the unit magnetization vector for each sublattice with the magnetization \vec{M}_i . The magnetic field $\vec{H}_i = -\frac{1}{\mu} \frac{\partial H}{\partial \vec{m}_i}$ is determined by the spin Hamiltonian:

$$H = - \sum_{i \neq j} J_{ij} \vec{m}_i \cdot \vec{m}_j + \sum_{i \neq j} \vec{d}_{ij} \cdot (\vec{m}_i \times \vec{m}_j) - K \sum_i (\hat{n}_i \cdot \vec{m}_i)^2, \quad (8)$$

where J_{ij} is the exchange coupling, \vec{d}_{ij} is the DMI vector, K is the magnetic anisotropy energy per Cr atom, and \hat{n}_i is the

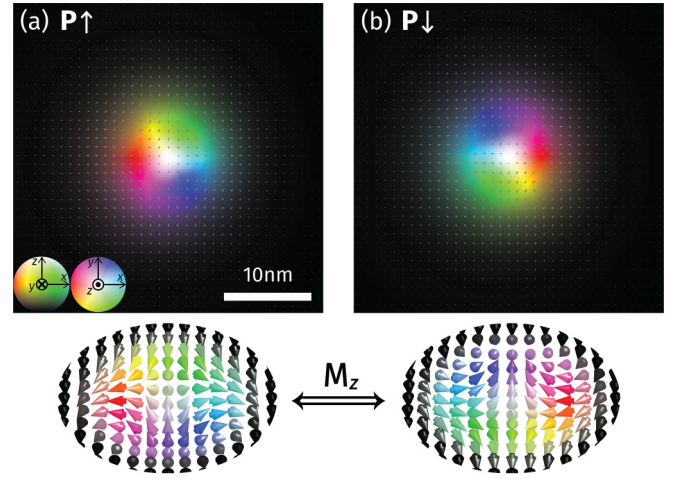


FIG. 6. (a), (b) Simulated antiskyrmion in polar bilayer $\text{Cr}_{0.88}\text{Mn}_{0.12}\text{I}_3$ with $P \uparrow$ (a) and $P \downarrow$ (b) for $K = 0.011$ MJ/m². Polarization switching is equivalent to mirror symmetry M_z transformation of the spin texture, resulting in its 90° rotation.

direction of the easy axis. Here, for simplicity, we neglect the magnetic-dipole interactions and the Kitaev-type anisotropic exchange coupling [82] based on the arguments articulated in Sec. VII and Supplemental Material [60]. We also ignore the next-nearest-neighbor DMI, due to its net contribution being canceled by symmetry of a CrI_3 monolayer.

In spin dynamics simulations, we consider all magnetic parameters to be the same as those given in Table I for $\text{Cr}_{0.88}\text{Mn}_{0.12}\text{I}_3$, except magnetic anisotropy K , which we assume to be variable in a small window between the calculated value $K = 0.04$ MJ/m³ (0.03 meV per atom) and $K = 0$. This approach is justified by the fact that a change is needed only by a fraction of a percent in Mn concentration to make the anisotropy zero. In this small range of the doping concentrations x , other magnetic parameters remain almost intact.

Our spin dynamics simulations indicate that an antiskyrmion emerges at $K < 0.014$ MJ/m². At $K = 0.011$ MJ/m², our results predict that an antiskyrmion has about 3.8 nm radius. Its shape and spin texture are shown in Fig. 6(a) for polarization of the bilayer pointing upward. It is seen that the antiskyrmion has the spin texture with Néel-type spin twists of opposite chirality along the x and y directions and Bloch-type spin twists of opposite chirality along the two diagonals.

In Fig. 5(b), we plot the calculated antiskyrmion radius as a function of magnetic anisotropy for the parameters of a $\text{Cr}_{0.88}\text{Mn}_{0.12}\text{I}_3$ polar bilayer. It is seen that the antiskyrmion radius [blue dots in Fig. 5(b)] decreases nearly linearly as anisotropy increases. For $K < 0.014$ MJ/m², an antiskyrmion disappears due to its size being reduced to the lattice constant, making it unstable. The decrease of the antiskyrmion size with increasing anisotropy is consistent with the prediction of Eq. (5) [orange curve in Fig. 5(b)]. However, Eq. (5) does not quantitatively reproduce the simulated R vs K curve, due to the antiskyrmion radius R being comparable to the domain-wall width w , breaking the limit of Eq. (5) applicability. Furthermore, for anisotropies that are smaller than $K_c = (\frac{\pi D}{4})^2/A$, the system can potentially realize antiskyrmion lattice, while the

spin dynamics simulations become unreliable in the vicinity of anisotropy K_c due to the divergent size of antiskyrmions.

As was noted above, an anisotropic DMI with $|D_{xy}| \neq |D_{yx}|$ is expected to produce elliptical antiskyrmions with the aspect ratio $\alpha = b/a \neq 1$, where a and b are the semimajor and semiminor axes of the ellipse, respectively. We do observe a deviation of the antiskyrmions from the spherical shape in our simulations. By fitting the polar angle variation of the spin profiles along x and y axes with the function [77,83]

$$\Theta(r) = 2\arctan\left[\frac{\sinh(R/w)}{\sinh(r/w)}\right], \quad (9)$$

where $R = a$ ($R = b$) along the semimajor y (semiminor x) axis, we obtain $a = 3.82$ nm and $b = 3.72$ nm for the antiskyrmion in Fig. 6. This implies that the aspect ratio is $\alpha \approx 0.97$, which agrees well with our estimate given by Eq. (6). It is notable that the aspect ratio does not simply scale with the ratio of D_{xy} and D_{yx} , which is $D_{xy}/D_{yx} \approx 0.77$ in our case, but is a more complex function of magnetic parameters D_{xy} , D_{yx} , K , and A , as follows from Eq. (6) (see Supplemental Material [60] for further details).

Importantly, the antiskyrmion spin texture can be controlled by the ferroelectric polarization orientation (Fig. 6). The $P \uparrow$ and $P \downarrow$ structures of a $\text{Cr}_{0.88}\text{Mn}_{0.12}\text{I}_3$ polar bilayer are related by mirror symmetry M_z transformation. This transformation changes the sign of DMI, resulting in switching spin chirality of the Néel- and Bloch-type twists [Fig. 6(b)]. The associated spin texture is transformed by flipping the in-plane component of spin which is equivalent to the 90° rotation of the antiskyrmion. This functionality may be useful for applications in nonvolatile spintronics and quantum computing [84].

VII. DISCUSSION

Our spin dynamics simulations do not take into account the magnetic-dipole interactions. It is known that these interactions break the circular symmetry of the antiskyrmion energy, affecting their stability and shape [28]. While skyrmions show a homochiral Néel spin texture, antiskyrmions exhibit both Néel and Bloch spin rotations. The latter do not produce magnetic charges, making the antiskyrmions energetically more stable. Also, the tendency to favor Bloch rotations over the Néel rotations distorts the spherical (elliptical) shape of antiskyrmions and facilitates the formation of square-shaped antiskyrmions, which have been observed experimentally [25–27]. While these effects are interesting, they are expected to emerge at antiskyrmion sizes well above 100 nm and should not influence much the results of our spin dynamics simulations. Also, dipolar interactions can stabilize larger-scale skyrmion-antiskyrmion pairs [85].

At elevated temperatures, thermal effects can make the antiskyrmions unstable and can lead to their disappearance. The antiskyrmion lifetime can be estimated from the equation $\tau = f_0^{-1} \exp(-\frac{\Delta E}{k_B T})$, where ΔE is the collapse energy barrier and f_0 is the attempt frequency which in 2D is related to temperature $f_0 \propto T$. Our micromagnetic simulations performed at different temperatures and fitted to this equation indicate that the barrier height is at least 20 K and could be as large as 40 K. Therefore, the predicted antiskyrmions can be observed at low temperature.

As was shown in our studies, MAE is the critical parameter which controls the antiskyrmion formation. Its reduction in CrI_3 was required to provide conditions for an antiskyrmion to occur. One could argue that the reduced magnetic anisotropy is expected for CrCl_3 and CrBr_3 , as compared to CrI_3 , due to a weaker spin-orbit coupling [79]. However, using these materials in a polar bilayer will likely be unfavorable for antiskyrmions because of the reduced DMI, which is scaled with spin-orbit coupling. Another possibility to reduce the magnetic anisotropy is to fabricate I-deficient CrI_3 , which is expected to provide e_g -electron doping and thus reduce the anisotropy. However, it is not obvious if the required stoichiometry of the CrI_{3-x} with a relatively large number of I vacancies can be achieved experimentally. The proposed Mn doping of CrI_3 seems to be the most viable option to reduce the perpendicular magnetic anisotropy and enhance the DMI.

Forming a moiré superlattice from a twisted AA-stacked bilayer is an interesting possibility that deserves to be further investigated. It has been recently predicted that a twisted CrX_3 ($X = \text{I, Br, Cl}$) bilayer exhibits an effective moiré exchange field resulting in a wide range of noncollinear magnetic phases that can be stabilized as a function of the twist angle in the presence of a nonzero DMI [86]. Making such a twisted bilayer polar using the approach proposed in this work creates conditions for a finite DMI. In this case, however, the DMI is expected to vary along the 2D system plane, which adds more complexity.

Overall, our work demonstrates that polar layer stacking of vdW 2D ferromagnets is an efficient method to generate and modulate DMI. Due to broken space inversion and in-plane rotation symmetries, a polar stacking-engineered bilayer provides necessary conditions for the emergence of magnetic quasiparticles, such as antiskyrmions. Cation doping can be used to tune the magnetic characteristics of the system to achieve the required magnetocrystalline anisotropy and DMI. The spin texture of antiskyrmions can be controlled by ferroelectric polarization in a nonvolatile fashion. Such functionality may be interesting for programmable skyrmion-based memories and logic.

Finally, it is worth noting that our proposed approach of using polar stacking as a means to generate the anisotropic DMI is not limited to the specific system but could be applicable to other 2D vdW ferromagnets. Additionally, polar layer stacking that breaks inversion and in-plane rotational symmetries makes it possible to generate other magnetic quasiparticles such as bimerons.

VIII. SUMMARY

In summary, based on first-principles DFT calculations, we have predicted the anisotropic DMI interaction in a CrI_3 bilayer engineered by polar layer stacking. Substitutional Mn doping was proposed to reduce the magnetocrystalline anisotropy of pristine CrI_3 to observe magnetic quasiparticles. Optimal conditions for the emergence of antiskyrmions were found in a polar $\text{Cr}_{0.88}\text{Mn}_{0.12}\text{I}_3$ bilayer, where a sizable DMI was predicted. Based on atomistic spin dynamics modeling, the formation of antiskyrmions was demonstrated, with the size tunable by Mn doping. A 90° rotation of the spin texture of magnetic antiskyrmions was predicted with reversal of ferroelectric polarization of the bilayer. This possibility of the

nonvolatile control of magnetic antiskyrmions in Mn doped CrI₃ by an applied electric field is promising for the potential device application of skyrmionic systems.

ACKNOWLEDGMENTS

This work was primarily supported by the Grant No. DE-SC0023140 funded by the U.S. Department of Energy, Office

of Science, Basic Energy Sciences (K.H., E.Y.T). E.S. and A.A.K. acknowledge support of the EPSCoR RII Track-1 program (NSF Award No. OIA-2044049) for performing the theoretical analysis of the (anti)skyrmion shape and size and effects of the Kitaev interaction. Computations were performed at the University of Nebraska Holland Computing Center.

- [1] A. N. Bogdanov and D. A. Yablonskii, Thermodynamically stable “vortices” in magnetically ordered crystals. The mixed state of magnets, *Zh. Eksp. Teor. Fiz.* **95**, 178 (1989) [*Sov. Phys. JETP* **68**, 101 (1989)].
- [2] S. Mühlbauer, B. Binz, F. Jonietz, C. Pfleiderer, A. Rosch, A. Neubauer, R. Georgii, and P. Böni, Skyrmion lattice in a chiral magnet, *Science* **323**, 915 (2009).
- [3] X. Z. Yu, Y. Onose, N. Kanazawa, J. H. Park, J. H. Han, Y. Matsui, N. Nagaosa, and Y. Tokura, Real-space observation of a two-dimensional skyrmion crystal, *Nature (London)* **465**, 901 (2010).
- [4] S. Heinze, K. von Bergmann, M. Menzel, J. Brede, A. Kubetzka, R. Wiesendanger, G. Bihlmayer, and S. Blügel, Spontaneous atomic-scale magnetic skyrmion lattice in two dimensions, *Nat. Phys.* **7**, 713 (2011).
- [5] W. Jiang, P. Upadhyaya, W. Zhang, G. Yu, M. B. Jungfleisch, F. Y. Fradin, J. E. Pearson, Y. Tserkovnyak, K. L. Wang, O. Heinonen, S. G. E. te Velthuis, and A. Hoffmann, Blowing magnetic skyrmion bubbles, *Science* **349**, 283 (2015).
- [6] O. Boulle, J. Vogel, H. Yang, S. Pizzini, D. de Souza Chaves, A. Locatelli, T. O. Montes, A. Sala, L. D. Buda-Prejbeanu, O. Klein M. Belmeguenai, Y. Roussigné, A. Stashkevich, S. M. Chérif, L. Aballe, M. Foerster, M. Chshiev, S. Auffret, I. M. Miron, and G. Gaudin, Room-temperature chiral magnetic skyrmions in ultrathin magnetic nanostructures, *Nat. Nanotechnol.* **11**, 449 (2016).
- [7] A. Fert, N. Reyren, and V. Cros, Magnetic skyrmions: Advances in physics and potential applications, *Nat. Rev. Mater.* **2**, 17031 (2017).
- [8] Y. Tokura, Magnetic skyrmion materials, *Chem. Rev.* **121**, 2857 (2021).
- [9] K. Everschor-Sitte, J. Masell, R. M. Reeve, and M. Kläui, Perspective: Magnetic skyrmions—Overview of recent progress in an active research field, *J. Appl. Phys.* **124**, 240901 (2018).
- [10] A. Fert, V. Cros, and J. Sampaio, Skyrmions on the track, *Nat. Nanotechnol.* **8**, 152 (2013).
- [11] G. Yu, P. Upadhyaya, Q. Shao, H. Wu, G. Yin, X. Li, C. He, W. Jiang, X. Han, P. K. Amiri, and K. L. Wang, Room-temperature skyrmion shift device for memory application, *Nano Lett.* **17**, 261 (2017).
- [12] S. Luo and L. You, Skyrmion devices for memory and logic applications, *APL Mater.* **9**, 050901 (2021).
- [13] N. Nagaosa and Y. Tokura, Topological properties and dynamics of magnetic skyrmions, *Nat. Nanotechnol.* **8**, 899 (2013).
- [14] P. Bruno, V. K. Dugaev, and M. Taillefumier, Topological Hall effect and Berry phase in magnetic nanostructures, *Phys. Rev. Lett.* **93**, 096806 (2004).
- [15] A. Neubauer, C. Pfleiderer, B. Binz, A. Rosch, R. Ritz, P. G. Niklowitz, and P. Böni, Topological Hall effect in the A phase of MnSi, *Phys. Rev. Lett.* **102**, 186602 (2009).
- [16] J. Zang, M. Mostovoy, J. H. Han, and N. Nagaosa, Dynamics of skyrmion crystals in metallic thin films, *Phys. Rev. Lett.* **107**, 136804 (2011).
- [17] W. Jiang, X. Zhang, G. Yu, W. Zhang, X. Wang, M. B. Jungfleisch, J. E. Pearson, X. Cheng, O. Heinonen, K. L. Wang, Y. Zhou, A. Hoffmann, and A. G. E. Te Velthuis, Direct observation of the skyrmion Hall effect, *Nat. Phys.* **13**, 162 (2017).
- [18] K. Litzius, I. Lemesh, B. Krüger, P. Bassirian, L. Caretta, K. Richter, F. Büttner, K. Sato, O. Tretiakov, J. Förster, R. M. Reeve, M. Weigand, I. Bykova, H. Stoll, G. Schütz, G. S. D. Beach, and M. Kläui, Skyrmion Hall effect revealed by direct time-resolved X-ray microscopy, *Nat. Phys.* **13**, 170 (2017).
- [19] A. A. Kovalev and S. Sandhoefner, Skyrmions and antiskyrmions in quasi-two-dimensional magnets, *Front. Phys.* **6**, 27 (2018).
- [20] I. Kézsmárki, S. Bordács, P. Milde, E. Neuber, L. M. Eng, J. S. White, H. M. Rønnow, C. D. Dewhurst, M. Mochizuki, K. Yanai, H. Nakamura, D. Ehlers, V. Tsurkan, and A. Loidl, Néel-type skyrmion lattice with confined orientation in the polar magnetic semiconductor GaV₄S₈, *Nat. Mater.* **14**, 1116 (2015).
- [21] M. Hoffmann, B. Zimmermann, G. P. Müller, D. Schürhoff, N. S. Kiselev, C. Melcher, and S. Blügel, Antiskyrmions stabilized at interfaces by anisotropic Dzyaloshinskii-Moriya interactions, *Nat. Commun.* **8**, 308 (2017).
- [22] I. Dzyaloshinsky, A thermodynamic theory of “weak” ferromagnetism of antiferromagnetics, *J. Phys. Chem. Solids* **4**, 4 (1958).
- [23] T. Moriya, Anisotropic superexchange interaction and weak ferromagnetism, *Phys. Rev.* **120**, 91 (1960).
- [24] A. K. Nayak, V. Kumar, T. Ma, P. Werner, E. Pippel, R. Sahoo, F. Damay, U. K. Röbler, C. Felser, and S. S. P. Parkin, Magnetic antiskyrmions above room temperature in tetragonal Heusler materials, *Nature (London)* **548**, 561 (2017).
- [25] L. C. Peng, R. Takagi, W. Koshibae, K. Shibata, K. Nakajima, T. Arima, N. Nagaosa, S. Seki, X. Z. Yu, and Y. Tokura, Controlled transformation of skyrmions and antiskyrmions in a non-centrosymmetric magnet, *Nat. Nanotechnol.* **15**, 181 (2020).
- [26] R. Saha, A. K. Srivastava, T. Ma, J. Jena, P. Werner, V. Kumar, C. Felser, and S. S. P. Parkin, Intrinsic stability of magnetic anti-skyrmions in the tetragonal inverse Heusler compound Mn_{1.4}Pt_{0.9}Pd_{0.1}Sn, *Nat. Commun.* **10**, 5305 (2019).
- [27] K. Karube, L. C. Peng, J. Masell, X. Z. Yu, F. Kagawa, Y. Tokura, and Y. Taguchi, Room-temperature antiskyrmions and

- sawtooth surface textures in a non-centrosymmetric magnet with S_4 symmetry, *Nat. Mater.* **20**, 335 (2021).
- [28] L. Camosi, N. Rougemaille, O. Fruchart, J. Vogel, and S. Rohart, Micromagnetics of antiskyrmions in ultrathin films, *Phys. Rev. B* **97**, 134404 (2018).
- [29] S. Huang, C. Zhou, G. Chen, H. Shen, A. K. Schmid, K. Liu, and Y. Wu, Stabilization and current-induced motion of antiskyrmion in the presence of anisotropic Dzyaloshinskii-Moriya interaction, *Phys. Rev. B* **96**, 144412 (2017).
- [30] C. Gong, L. Li, Z. Li, H. Ji, A. Stern, Y. Xia, T. Cao, W. Bao, C. Wang, Y. Wang, Z. Q. Qiu, R. J. Cava, S. G. Louie, J. Xia, and X. Zhang, Discovery of intrinsic ferromagnetism in two-dimensional van der Waals crystals, *Nature (London)* **546**, 265 (2017).
- [31] B. Huang, G. Clark, E. Navarro-Moratalla, D. R. Klein, R. Cheng, K. L. Seyler, D. Zhong, E. Schmidgall, M. A. McGuire, D. H. Cobden, W. Yao, D. Xiao, P. Jarillo-Herrero, and X. Xu, Layer-dependent ferromagnetism in a van der Waals crystal down to the monolayer limit, *Nature (London)* **546**, 270 (2017).
- [32] Z. Fei, B. Huang, P. Malinowski, W. Wang, T. Song, J. Sanchez, W. Yao, D. Xiao, X. Zhu, A. F. May, W. Wu, D. H. Cobden, J. Chu, and X. Xu, Two-dimensional itinerant ferromagnetism in atomically thin Fe_3GeTe_2 , *Nat. Mater.* **17**, 778 (2018).
- [33] Y. Deng, Y. Yu, Y. Song, J. Zhang, N. Z. Wang, Z. Sun, Y. Yi, Y. Z. Wu, S. Wu, J. Zhu, J. Wang, X. H. Chen, and Y. Zhang, Gate-tunable room-temperature ferromagnetism in two-dimensional Fe_3GeTe_2 , *Nature (London)* **563**, 94 (2018).
- [34] I. Žutić, A. Matos-Abiad, B. Scharf, H. Dery, and K. Belashchenko, Proximitized materials, *Mater. Today* **22**, 85 (2019).
- [35] K. Huang, D.-F. Shao, and E. Y. Tsymlal, Ferroelectric control of magnetic skyrmions in two-dimensional van der Waals heterostructures, *Nano Lett.* **22**, 3349 (2022).
- [36] T.-E. Park, L. Peng, J. Liang, A. Hallal, F. S. Yasin, X. Zhang, K. M. Song, S. J. Kim, K. Kim, M. Weig, G. Schütz, S. Finizio, J. Raabe, K. Garcia, J. Xia, Y. Zhou, M. Ezawa, X. Liu, J. Chang, H. C. Koo, Y. D. Kim, M. Chshiev, A. Fert, H. Yang, X. Yu, and S. Woo, Néel-type skyrmions and their current-induced motion in van der Waals ferromagnet-based heterostructures, *Phys. Rev. B* **103**, 104410 (2021).
- [37] B. Ding, Z. Li, G. Xu, H. Li, Z. Hou, E. Liu, X. Xi, F. Xu, Y. Yao, and W. Wang, Observation of magnetic skyrmion bubbles in a van der Waals ferromagnet Fe_3GeTe_2 , *Nano Lett.* **20**, 868 (2020).
- [38] Y. Wu, S. Zhang, J. Zhang, W. Wang, Y. L. Zhu, J. Hu, G. Yin, K. Wong, C. Fang, C. Wan, X. Han, Q. Shao, T. Taniguchi, K. Watanabe, J. Zang, Z. Mao, X. Zhang, and K. L. Wang, Néel-type skyrmion in $\text{WTe}_2/\text{Fe}_3\text{GeTe}_2$ van der Waals heterostructure, *Nat. Commun.* **11**, 3860 (2020).
- [39] M. Yang, Q. Li, R. V. Chopdekar, R. Dhall, J. Turner, J. D. Carlström, C. Ophus, C. Klewe, P. Shafer, A. T. N'Diaye, J. W. Choi, G. Chen, Y. Z. Wu, C. Hwang, F. Wang, and Z. Q. Qiu, Creation of skyrmions in van der Waals ferromagnet Fe_3GeTe_2 on $(\text{Co}/\text{Pd})_n$ superlattice, *Sci. Adv.* **6**, eabb5157 (2020).
- [40] Y. Wu, B. Francisco, Z. Chen, W. Wang, Y. Zhang, C. Wan, X. Han, H. Chi, Y. Hou, A. Lodesani, G. Yin, K. Liu, Y.-T. Cui, K. L. Wang, and J. S. Moodera, A van der Waals interface hosting two groups of magnetic skyrmions, *Adv. Mater.* **34**, 2110583 (2022).
- [41] K. Yasuda, X. Wang, K. Watanabe, T. Taniguchi, and P. Jarillo-Herrero, Stacking-engineered ferroelectricity in bilayer boron nitride, *Science* **372**, 1458 (2021).
- [42] M. V. Stern, Y. Waschita, W. Cao, I. Nevo, K. Watanabe, T. Taniguchi, E. Sela, M. Urbakh, O. Hod, and M. B. Shalom, Interfacial ferroelectricity by van der Waals sliding, *Science* **372**, 1462 (2021).
- [43] Y. Cao, V. Fatemi, S. Fang, K. Watanabe, T. Taniguchi, E. Kaxiras, and P. Jarillo-Herrero, Unconventional superconductivity in magic-angle graphene superlattices, *Nature (London)* **556**, 43 (2018).
- [44] Z. Zheng, Q. Ma, Z. Bi, S. de la Barrera, M.-H. Liu, N. Mao, Y. Zhang, N. Kiper, K. Watanabe, T. Taniguchi, J. Kong, W. A. Tisdale, R. Ashoori, N. Gedik, L. Fu, S.-Y. Xu, and P. Jarillo-Herrero, Unconventional ferroelectricity in moiré heterostructures, *Nature (London)* **588**, 71 (2020).
- [45] Y. Xie, A. T. Pierce, J. M. Park, D. E. Parker, E. Khalaf, P. Ledwith, Y. Cao, S. H. Lee, S. Chen, P. R. Forrester, K. Watanabe, T. Taniguchi, A. Vishwanath, P. Jarillo-Herrero, and A. Yacoby, Fractional Chern insulators in magic-angle twisted bilayer graphene, *Nature (London)* **600**, 439 (2021).
- [46] L. Li and M. Wu, Binary compound bilayer and multilayer with vertical polarizations: Two-dimensional ferroelectrics, multiferroics, and nanogenerators, *ACS Nano* **11**, 6382 (2017).
- [47] L.-P. Miao, N. Ding, N. Wang, C. Shi, H.-Y. Ye, L. Li, Y.-F. Yao, S. Dong, and Y. Zhang, Direct observation of geometric and sliding ferroelectricity in an amphidynamic crystal, *Nat. Mater.* **21**, 1158 (2022).
- [48] E. Y. Tsymlal, Two-dimensional ferroelectricity by design, *Science* **372**, 1389 (2021).
- [49] T. Cao, D.-F. Shao, K. Huang, G. Gurung, and E. Y. Tsymlal, Switchable anomalous Hall effects in polar-stacked 2D antiferromagnet MnBi_2Te_4 , *Nano Lett.* **23**, 3781 (2023).
- [50] S. Jiang, L. Li, Z. Wang, K. F. Mak, and J. Shan, Controlling magnetism in 2D CrI_3 by electrostatic doping, *Nat. Nanotechnol.* **13**, 549 (2018).
- [51] D. R. Klein, D. MacNeill, J. L. Lado, D. Soriano, E. Navarro-Moratalla, K. Watanabe, T. Taniguchi, S. Manni, P. Canfield, J. Fernández-Rossier, and P. Jarillo-Herrero, Probing magnetism in 2D van der Waals crystalline insulators via electron tunneling, *Science* **360**, 1218 (2018).
- [52] T. Li, S. Jiang, N. Sivadas, Z. Wang, Y. Xu, D. Weber, J. E. Goldberger, K. Watanabe, T. Taniguchi, C. J. Fennie, K. F. Mak, and J. Shan, Pressure-controlled interlayer magnetism in atomically thin CrI_3 , *Nat. Mater.* **18**, 1303 (2019).
- [53] A. K. Behera, S. Chowdhury, and S. R. Das, Magnetic skyrmions in atomic thin CrI_3 monolayer, *Appl. Phys. Lett.* **114**, 232402 (2019).
- [54] R. A. Beck, L. Lu, P. V. Sushko, X. Xu, and X. Li, Defect-induced Magnetic skyrmion in a two-dimensional chromium triiodide monolayer, *JACS Au* **1**, 1362 (2021).
- [55] M. A. McGuire, H. Dixit, V. R. Copper, and B. C. Sales, Coupling of crystal structure and magnetism in the layered, ferromagnetic insulator CrI_3 , *Chem. Mater.* **27**, 612 (2015).
- [56] P. Jiang, C. Wang, D. Chen, Z. Zhong, Z. Yuan, Z.-Y. Lu, and W. Ji, Stacking tunable interlayer magnetism in bilayer CrI_3 , *Phys. Rev. B* **99**, 144401 (2019).
- [57] F. Xue, Y. Hou, Z. Wang, and R. Wu, Two-dimensional ferromagnetic van der Waals CrCl_3 monolayer with enhanced

- anisotropy and Curie temperature, *Phys. Rev. B* **100**, 224429 (2020).
- [58] S. Laref, K.-W. Kim, and A. Manchon, Elusive Dzyaloshinskii-Moriya interaction in monolayer Fe_3GeTe_2 , *Phys. Rev. B* **102**, 060402(R) (2020).
- [59] H. Yang, A. Thiaville, S. Rohart, A. Fert, and M. Chshiev, Anatomy of Dzyaloshinskii-Moriya interaction at Co/Pt interfaces, *Phys. Rev. Lett.* **115**, 267210 (2015).
- [60] See Supplemental Material at <http://link.aps.org/supplemental/10.1103/PhysRevB.109.024426> for orbital-resolved density of states of $\text{Cr}_{1-x}\text{Mn}_x\text{I}_3$ bilayers, theoretical analysis and method of calculation of the DMI vectors and the DMI tensor, analytic expressions for the (anti)skyrmion shape and size, and the effect of the Kitaev interaction.
- [61] S. Sandhoefner, A. Raeliarijaona, R. Nepal, D. Snyder-Tinoco, and A. A. Kovalev, Regular and in-plane skyrmions and antiskyrmions from boundary instabilities, *Phys. Rev. B* **104**, 064417 (2021).
- [62] K. Shibata, J. Iwasaki, N. Kanazawa, S. Aizawa, T. Tanigaki, M. Shirai, T. Nakajima, M. Kubota, M. Kawasaki, H. S. Park, D. Shindo, N. Nagaosa, and Y. Tokura, Large anisotropic deformation of skyrmions in strained crystal, *Nat. Nanotechnol.* **10**, 589 (2015).
- [63] G. Kresse and D. Joubert, From ultrasoft pseudopotentials to the projector augmented-wave method, *Phys. Rev. B* **59**, 1758 (1999).
- [64] G. Kresse and J. Furthmüller, Efficient iterative schemes for ab initio total-energy calculations using a plane-wave basis set, *Phys. Rev. B* **54**, 11169 (1996).
- [65] J. P. Perdew, A. Ruzsinszky, G. I. Csonka, O. A. Vydrov, G. E. Scuseria, L. A. Constantin, X. Zhou, and K. Burke, Restoring the density-gradient expansion for exchange in solids and surfaces, *Phys. Rev. Lett.* **102**, 039902 (2009).
- [66] S. L. Dudarev, A. G., S. V. Savrasov Botton, C. J. Humphreys, and A. P. Sutton, Electron-energy-loss spectra and the structural stability of nickel oxide: An LSDA+U study, *Phys. Rev. B* **57**, 1505 (1998).
- [67] R. F. L. Evans, W. J. Fan, P. Chureemart, T. A. Ostler, M. O. A. Ellis, and R. W. Chantrell, Atomistic spin model simulations of magnetic nanomaterials, *J. Phys.: Condens. Matter* **26**, 103202 (2014).
- [68] D. Šabani, C. Bacaksiz, and M. V. Milošević, Ab initio methodology for magnetic exchange parameters: Generic four-state energy mapping onto a Heisenberg spin Hamiltonian, *Phys. Rev. B* **102**, 014457 (2020).
- [69] J. L. Lado and J. Fernández-Rossier, On the origin of magnetic anisotropy in two dimensional CrI_3 , *2D Mater.* **4**, 035002 (2017).
- [70] J. Liu, M. Shi, and M. P. Anantram, Analysis of electrical-field-dependent Dzyaloshinskii-Moriya interaction and magnetocrystalline anisotropy in a two-dimensional ferromagnetic monolayer, *Phys. Rev. B* **97**, 054416 (2018).
- [71] Q. Tong, F. Liu, J. Xiao, and W. Yao, Skyrmions in the Moiré of van der Waals 2D magnets, *Nano Lett.* **18**, 7194 (2018).
- [72] T. R. Paudel and E. Y. Tsybal, Spin filtering in CrI_3 tunnel junctions, *ACS Appl. Mater. Int.* **11**, 15781 (2019).
- [73] D. Wang and B. Sanyal, Systematic study of monolayer to trilayer CrI_3 : Stacking sequence dependence of electronic structure and magnetism, *J. Phys. Chem. C* **125**, 18467 (2021).
- [74] B. Sadhukhan, A. Bergman, Y. O. Kvashnin, J. Hellsvik, and A. Delin, Spin-lattice couplings in two-dimensional CrI_3 from first-principles computations, *Phys. Rev. B* **105**, 104418 (2022).
- [75] N. Sivadas, S. Okamoto, X. Xu, C. J. Fennie, and D. Xiao, Stacking-dependent magnetism in bilayer CrI_3 , *Nano Lett.* **18**, 7658 (2018).
- [76] A. Vansteenkiste, J. Leliaert, M. Dvornik, M. Helsen, F. Garcia-Sanchez, and B. V. Waeyenberge, The design and verification of MuMax3, *AIP Adv.* **4**, 107133 (2014).
- [77] X. S. Wang, H. Y. Yuan, and X. R. Wang, A theory on skyrmion size, *Commun. Phys.* **1**, 31 (2018).
- [78] Q. Sun and N. Kioussis, Prediction of manganese trihalides as two-dimensional Dirac half-metals, *Phys. Rev. B* **97**, 094408 (2018).
- [79] B. Yang, X. Zhang, H. Yang, X. Han, and Y. Yan, Nonmetallic atoms induced magnetic anisotropy in monolayer chromium trihalides, *J. Phys. Chem. C* **123**, 691 (2019).
- [80] P. W. Anderson, Antiferromagnetism. Theory of superexchange interaction, *Phys. Rev.* **79**, 350 (1950).
- [81] H. Wang, F. Fan, S. Zhu, and H. Wu, Doping enhanced ferromagnetism and induced half-metallicity in CrI_3 monolayer, *EPL* **114**, 47001 (2016).
- [82] C. Xu, J. Feng, H. Xiang, and L. Bellaiche, Interplay between Kitaev interaction and single ion anisotropy in ferromagnetic CrI_3 and CrGeTe_3 monolayers, *npj Comput. Mater.* **4**, 57 (2018).
- [83] H.-B. Braun, Fluctuations and instabilities of ferromagnetic domain-wall pairs in an external magnetic field, *Phys. Rev. B* **50**, 16485 (1994).
- [84] J. Xia, X. Zhang, X. Liu, Y. Zhou, and M. Ezawa, Universal quantum computation based on nanoscale skyrmion helicity qubits in frustrated magnets, *Phys. Rev. Lett.* **130**, 106701 (2023).
- [85] H. Wang, F. Fan, S. Zhu, and H. Wu, Theory of antiskyrmions in magnets, *Nat. Commun.* **7**, 10542 (2016).
- [86] M. Akram, H. LaBollita, D. Dey, J. Kapeghian, O. Erten, and A. S. Botana, Moiré skyrmions and chiral magnetic phases in twisted CrX_3 ($X = \text{I, Br, and Cl}$) bilayers, *Nano Lett.* **21**, 6633 (2021).